Experiments on lift dynamics and feedback control of a wind turbine blade section

V. Jaunet, C. Braud

Accepted Manuscript

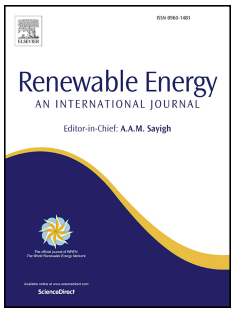

Experiments on lift dynamics and feedback control of a wind turbine blade section

V. Jaunet, C. Braud

PII: S0960-1481(18)30322-7

DOI: 10.1016/j.renene.2018.03.017

Reference: RENE 9886

To appear in: *Renewable Energy*

Received Date: 1 August 2017

Revised Date: 8 March 2018

Accepted Date: 9 March 2018

Please cite this article as: Jaunet V, Braud C, Experiments on lift dynamics and feedback control of a wind turbine blade section, *Renewable Energy* (2018), doi: 10.1016/j.renene.2018.03.017.

Experiments on lift dynamics and feedback control of a wind turbine blade section

V. Jaunet, C. Braud

LHEEA lab. - CNRS - Ecole Centrale Nantes
1 rue de la Noë,
44100 Nantes

Abstract

An experimental campaign is performed to the study of feedback lift control applied to a wind turbine blade. A 5-digit NACA profile whose trailing edge is rounded for circulation control purposes is used in combination with fluidic actuation. It is first shown in this article how the modified profile performs, in terms of aerodynamic forces, in both natural and manipulated cases. Then, the dynamics of controlled pressure (and thus lift) establishment is identified. A discussion is given on the speed of lift dynamics in comparison with previous studies and on its ability to overcome lift perturbations due to external perturbations. Finally, a feedback lift control experiment is performed showing the feasibility of such control in a wind turbine environment.

Keywords: Feedback control, Wind turbine, Lift

1. Introduction

Wind turbines evolve in the atmospheric boundary layer at a height where strong wind velocity fluctuations in both amplitude and direction can be found [1]. These fluctuations not only modify the actual forces acting on the blade but can also lead to dynamic stall [2, 3], therefore creating undesirable mechanical loads on the turbine that can lead to severe damages. Controlling the lift of the individual wind turbine blades may thus be considered to soften these undesired

forces.

Recently, Choudhry et al. [4] proposed to manipulate the flow using passive actutator to reduce the lift pertubation due to dynamic stall. Although the use of passive actuators revealed to be efficient in this purpose, it may be difficult to optimize their design for a variety of flow regimes. Moreover, the fact that they have to be permanently installed may cause efficiency penalty at standard functionning regime that might not be accepted by manufacturers and energy producers. Flaps and slats are also considered for this purpose [5, 6, 7, 8] but additional moving parts, even very efficient, are often discarded by manufacturers due to the plausible additional maintenance costs. On the other hand, Active Flow Control (AFC) devices, such as systems using air injection to manipulate lift, has received a lot of attention in aeronautic applications to achieve a lighter and mechanically simpler high lift systems for transonic commercial transport aircraft [9].

Since the early work of Englar and Williams [10] and Englar [12, 11], circulation control (CC) using secondary injection and Coanda effect at the trailing edge is known to produce an efficient way of modifying the lift of a wing profile. The lift gain produced by Coanda jet circulation control is obtained through two mechanisms. The main one is the displacement of the stagnation points at the leading edge and trailing edge, hence changing the circulation around the wing [11]. The second one is through suction by the very low wall pressure that the Coanda turning can produce on the Coanda surface [13]. Circulation control using Coanda effect has been investigated for a great variety of field from helicopter blades to propellers, showing the great interest of the research community in such techniques [14]. However, circulation control using Coanda has only recently been investigated in the field of wind turbine aerodynamics [15, 16, 17, 18, 19]. Cagle and Jones [20] and Jones et al. [21] provided experimental feasability evidence of CC on wing profiles similar to the one used on wind turbines but only gave steady-state information on the system. To the author's knowledge, few studies aimed at revealing the dynamics of lift enhancement by means of circulation control systems while this is an essential

information for control purposes.

Closed-loop control of the blade lift must be considered to dynamically alleviate the mechanical loads due to wind gusts. Closed-loop lift control has been of great interest especially for post-stall performance recovery of aircraft airfoils. Williams et al. [22, 23] used leading edge actuation to recover lift on a 3D airfoil after separation of the boundary layer. Colonius and Williams [24] puts forward that the dynamics response of lift shows some universal features, whatever the actuation or the type of profile of interest [25, 23]. They observed a response time of about a dozen of chord convective time $t^* = C/U_\infty$, where C is the chord and U_∞ is the freestream velocity. The same order of magnitude is also observed by Darabi and Wygnanski [26, 27] in a separated flow over a flap, by Mathis et al. [28] for a separation on a bevelled trailing edge and by Shaqarin et al. [29] in a thick separated boundary layer over a flap. Moreover, it is generally observed that a pulsed fluidic actuation has increased performances compared to a continuous fluidic actuation [21, 29]. Initial vorticity when the jet is blown might explain the extra suction obtained by pulsed jets. Similar to the observation of initial lift gain of controlled stalled airfoils made by Colonius and Williams [24]. It seems nevertheless that the research effort in closed-loop lift control has mainly been focused on post-stall lift recovery.

Recently, Troshin and Seifert [30] performed closed-loop lift control on an airfoil with distributed fluidic actuation on the suction side of an unstalled thick wing, aiming at the recovery of lift loss due to surface degradation. They observed the lift to respond as a second order system with a typical response time of 8.1 convective chord time (*i.e.* in the same order of magnitude of the stalled cases). They also showed that the system dynamics may vary with both the Reynolds number and the angle of attack (AOA). The higher is the AOA, the higher is the gain, with a possibly faster response when AOA or Reynolds number increases (it is not possible to distinguish AOA and Reynolds number effects from their results).

Therefore, the aim of this paper is to provide a steady-state as well a dynamical information of lift control of a wind turbine blade profile whose trailing

edge is modified to allow circulation control. The control objective is to compensate atmospheric perturbations from manipulation of the lift, and closed-loop control is considered to dynamically maintain this objective. The experimental apparatus is described in the section II, then the average natural and actuated flow fields are described using PIV results in section III, providing information on the actuation functioning. In section IV we provide steady state information on lift control. Section V is dedicated to the dynamics of lift control in both open- and closed-loop configurations. Concluding remarks are given in section VI.

2. Experimental set-up

2.1. Blade profile

The trailing edge of a $NACA-65_4421$ airfoil profile has been rounded (radius of curvature 2% of the chord) and the camber of the airfoil has been adjusted to compensate aerodynamic degradation due to the round trailing edge. The profile is presented in figure 1 (left). The standard NACA-65(4)421 profile is a thick profile with two C_L drops corresponding to a first boundary layer separation at the trailing edge of the profile for $AOA \simeq 8^\circ$, called latter α_{sep}, and a second strong flow separation at the leading edge for $AOA \simeq 20^\circ$ [31]. From α_{sep} to 20° the separation point moves gradually from the trailing edge to the leading edge, corresponding to a gradual variation of the loads. As can be seen in figure 1, this is also the case for the modified NACA-65(4)421 of the present work as shown by Baléria [32] and Aubrun and Leroy [33]. The relation between the two C_L drops and the flow separation state of the current profile has been investigated by Baléria [32] using PIV measurements. We focus our work on AOA where only trailing edge separation occurs($AOA \simeq \alpha_{sep}{}^\circ$ but $AOA << 20^\circ$). The figure 1 also shows that the geometrical modifications of the blade lead to an overall increase in lift due to the additionnal camber. Apart from that, the modified wing lift behaves in a similar manner than the original

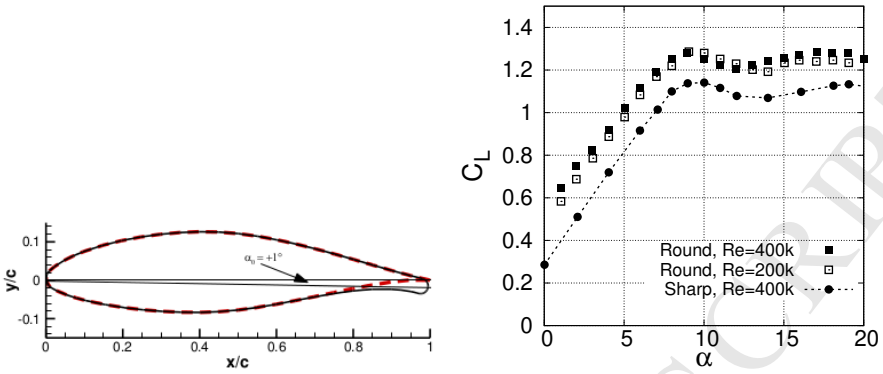

Figure 1: (Right) Arifoil profile. The original $NACA - 65_4421$ airfoil is in red dash line and the control profile $NACA - 65_4421 - CC$, used in this study, is in solid black line. (Left) modified profile aerodynamic performances from Aubrun and Leroy [33].

wing.

The discrete microjets are distributed along the wing span from the stack of thin profiles (1 mm spanwise) and thick blind profiles (20mm spanwise). The thin profiles possess a round hole connected to a small air circuit (of 1 mm width) open to the surface of the profile. This is illustrated in figure 2 (Left). The thick profile possess the same round hole with no connection to the surface. Once stacked, the holes form a plenum chamber in the span direction of the profile, which can be connected to pressurized air to generate discrete squared fluidic microjets. The same principle is reversely used to measure the pressure distribution around the chord. The measured pressure is hence integrated along the span of the profile, providing results close to what can be obtained in a 2D pressure field.

2.2. Wind tunnel

The measurements are conducted at the University of Orléans, in the Lucien Malavard closed return wind tunnel of the PRISME laboratory. The test section of 5 m long with a cross-section of 2 m x 2 m. The turbulence level in this test

Figure 2: Left: diagram of a thin (non-blind) profile. Right:photograph of the thick (blind) and thin (non-blind) profiles.

section is below 0.4% and the operating speed of the wind tunnel is set to $U_\infty = 10m/s$ in the present study. The 2D blade is mounted between two vertical flat planes in order to achieve a 2D flow configuration. The wing span was equal to the distance between these two plates and measured $L = 1.1$m. At this free stream velocity, the Reynolds number of the flow based on the chord length ($C = 0.3$ m) is slightly above 2×10^5.

2.2.1. Unsteady angle of attack

A step in Reynolds number would be pefectly suited to model a gust effect. However, it is not trivial to perform a wind step with a standard wind tunnel. At the blade scale, a simple steady shear inflow in front of a wind turbine rotor disk induces a cycling variation of the blade incidence [34]. Therefore, some aerodynamic facilities have modeled mean wind shear inflows effects using an active rotation of the wing [3]. Also, additional devices can be used at the inlet of the test section to explore different slow harmonic perturbations [35]. These studies do not however take into account the additional impact of small turbulence scales. Impact of free-stream turbulence has been investigated for the present NACA profile by Devinant et al. [31]. They show that high turbulence levels have a major effect on aerodynamic properties when the separation point moves from the trailing edge to the leading edge ($AOA > 8^\circ$). At the rotor scale, active grids are nowadays used to reproduce spectral features similar to those found in the atmospheric boundary layer [36]. These perturbations can adequately model stationary mean and turbulent flow properties of atmospheric

turbulent flows. A the time of writing this article, a perturbation system is under development in our wind tunnel facility to take into account the impact of more realistic gust conditions on the control efficiency. However, a first simplified approach is considered in the present work. The wing is mounted on a specific bench that automatically controls the AoA of the wing to simulate a constant shear inflow in front of the wind turbine rotor. We focus on the linear part of the lift curve ($AOA < 8^\circ$) with only modest explorations towards AoA for which the flow separates at the trailing edge (i.e. $AOA \simeq 10^\circ$ but $AoA << 20^\circ$).

The wing can oscillate at a chosen frequency and amplitude of the incidence, around a specified AOA. The maximum allowed frequency is 1 Hz (or $St_{max} = \frac{fC}{U} = 0.03$) and a maximum amplitude of 6° was used in the present study.

2.3. Air delivery system

The compressed air circuit delivering the air to the actuator is composed of a pressure regulator, a plenum tank and the actuation is monitored through the help of electric valves. The pressure regulator is used to expand the incomming compressed air to a given pressure, monitoring the actuation intensity by setting the microjet stagnation pressure. The expanded air is then stocked in an intermediate plenum tank working as a decoupling capacitor, ensuring the stability of the actuator stagnation pressure while the flow is rapidly set when opening the valves. The momentum coefficient C_μ is used as a measure of the actuation strength. It is defined as :

$$C_\mu = \frac{Q_{\mu j} V_{\mu j}}{1/2 \rho_\infty U_\infty^2 S_{ref}}, \tag{1}$$

where, $Q_{\mu j}$ is the injection mass flow rate, $V_{\mu j}$ is the injected flow velocity, $S_{ref} = C \cdot L$ is the reference area of the wing, and the subscript ∞ refers to the external flow conditions. It is straightforward to show that:

$$C_\mu = 2 \cdot \frac{P_{\mu j} M_{\mu j}^2}{P_\infty M_\infty^2} \cdot \frac{S_{\mu j}}{S_{ref}}, \tag{2}$$

where $P_{\mu j}$ is the static pressure of the microjet at the exit section, $M_{\mu j}$ is the exit Mach number of the microjet and $S_{\mu j}$ the exit section area of the actuators. The present experimental set-up allows to vary C_μ from 0 to 0.14.

As long as the injection stays subsonic, $P_{\mu j}$ is equal to the pressure at the location of the actuator. Hence, at constant incoming flow conditions, fixed AOA and fixed microjet exit section, C_μ solely depends on the ratio of microjet to external Mach numbers $M_{\mu j}/M_\infty$. This ratio can only be changed by increasing the stagnation pressure of the micro-jet. The relationship between C_μ and the stagnation pressure of the micro-jets is theoretically non-linear, but in the limited range of $M_{\mu j}$ that could be set in the present experiment C_μ can be well approximated by a linear function of the microjet stagnation pressure.

Note that we used the compressible form of the C_μ because the micro-jet Mach number can easily exceed $M_{\mu j} = 0.3$ (the respective stagnation to static pressure ratio is 1.064). Furthermore, since $M_{\mu j}$ is directly obtained from the isentropic relations, there is no need to know the temperature of the microjet flow to compute the C_μ, which makes this formulation easier to use.

2.4. Measurement apparatus

2.4.1. Balance

First, the profile was placed on a 6-axis balance system to measure the time averaged lift and drag. The balance was carefully calibrated so that lift and drag uncertainties were estimated to be less than 2% in the free stream velocity range used in this study.

2.4.2. Wall pressure sensing

Two sets of pressure transducers were used during the experiments. The first one was used during the open loop characterization of the lift dynamics. The pressure taps were then connected to two Chell MicroDAQ pressure scanners to synchronously obtain the pressure field around the profile. The scanners were externally triggered at 500Hz, the maximum possible sampling frequency

with this configuration. Note that this sampling frequency is fast enough with respect to the characteristic time scales of interest in this paper. At each rising edge of the trigger signal, the pressure scanner performed an acquisition of all the channels and sent the digital values over the network to a dedicated computer. The number of received samples were compared to the number of rising edges to control that no packet losses were encountered.

The closed loop controler we used was integrated in a PC running a Linux OS with a RT_PREEMPT patch for hard real time performances. This computer was equipped with an ADC PCI board for the input-output purposes. The expected input of this controler is analog voltage values from pressure transducers. Since the pressure scanners embed their own ADC, it was not possbile to use them in our feedback-loop. Therefore a set of 16 FirstSensor analog pressure transducers was used, allowing to measure the pressure using a standard acquisition board on a PC. These sensors have a response frequency of 2kHz, sligthly faster than the pressure scanners.

2.4.3. PIV

The flow field around the actuator was probed using Particle Image Velocimetry (PIV). A 2D-2C PIV system was used for cross-sections of the profile (see figure 3 (Left)). The measurements were performed at different spanwise locations. Additionally, a 2D-3C Stereo-PIV system was used to measure the flow field downstream of the trailing edge, at several streamwise locations (see figure 3 (Right)). In both cases the cameras and the laser were placed on a traverse system allowing to change the measurement position without modify the calibration.

The PIV systems were constituted of 16 Mpixels Imperx CCD cameras and a 200 mJ Quantel EverGreen laser. The maximum PIV acquisition rate could be set at 4Hz. The imaging was done through Nikon 200mm f#4 Macro lenses set at their widest opening f#4. The chosen field of view was about 200mm wide ($0.66C$) in all cases, this gives a diffraction limited particle image size of

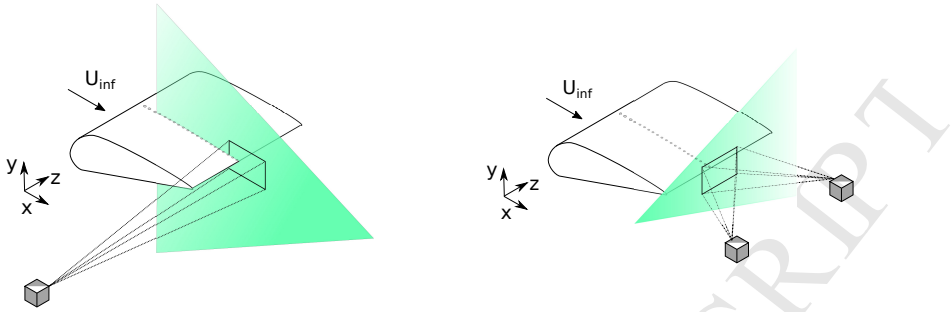

Figure 3: Diagram of the experimental arrangement showing the location of the PIV measurement volume in the 2D-2C configuration (left) and in the 2D-3C configuration (right)

6 μm slightly smaller than the pixel size [37]. Nevertheless, thanks to the sufficient amount of light provided by the 200 mJ laser, the actual particle images were bigger and no sign of peak-locking could be observed in the data. The flow was seeded with olive oil particles generated through Lazkin nozzles. Their averaged diameter is less than 1 μm giving a response time of 2 μs which is sufficient for the time scales of interest in this paper. We set the inter-frame time accordingly to the maximum displacement and/or out of plane motion to maximize both the measurement accuracy and the cross-correlation value. The inter-frame time ranged from 5 to 20μs.

For the Stereo-PIV the lenses were mounted to the cameras with Scheimpflug adaptors. It was possible to set both camera at a 45 degree viewing angle, ensuring that measurement errors are well balanced between all the velocity components [38, 39].

The PIV image processing was performed using an iterative algorithm with deforming interrogation windows [40, 41] and seeding adaptivity [42]. The initial window size was set at 32x32 pixels with an overlap of 50%. Outliers were rejected using a correlation peak-ratio of 1.3 together with a Universal Outlier Detection spatial filter [43]. The processing was carried out in both *Davis 8.2* from *LaVision* and *DynamicStudio 2016a* from *Dantec Dynamics*. The PIV was running at full speed and a set of 1000 PIV fields were taken for each actuation intensity and measurement volume location.

2.4.4. Synchronization

Given the numerous different measurements types, with their respective performances, that had to be performed synchronously, a dedicated triggering device was designed. The trigger signals for the PIV, the pressure sampling and the actuation systems were generated using the internal timers and pulse width modulation capabilities of an Atmel atmega2560 microcontroler. In the meantime, the trigger signals (for the pressure reccording and the PIV) as well as the PIV laser Q-switch signals were recorded on an independant ADC system to *a posteriori* synchronize the data sets obtained at different sampling frequencies. The acquistion of these signals was performed at 20kHz.

3. Flow field description/Mean spatial organization

3.1. Mean velocity field

3.1.1. Streamwise flow field

We present in figure 4 the average streamwise and vertical velocity components of the flow measured in the $z = 0$ plane around the trailing edge for three different momentum coefficients. The velocity is normalized by the free stream velocity U_∞. Note that this velocity scale might not be appropriate to reflect the microjet exit velocity, which is expected to be an order of magnitude higher than the freestream one.

The base flow ($C_\mu = 0$, top row) is characterized by the existence of a recirculating zone with two counter rotating cells. These cells can be deduced from the presence of the two positive and negative vertical velocity contours as well as the negative streamwise velocity contour circled by the black line representing the $U = 0$ isoline, just behind the trailing edge of the wing. Note that the negative streamwise velocity contour were saturated to enhance the visibility of the recirculation bubble. This is typical of bluff body wakes and is present in our case because of the rounded trailing edge of the wing. The recirculating flow

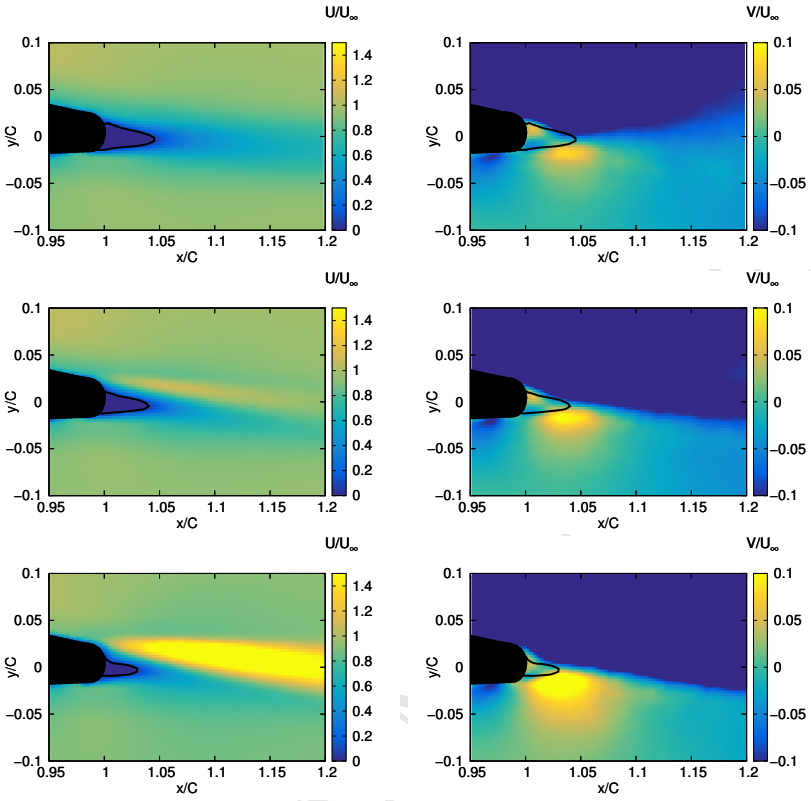

Figure 4: Isocontours of the averaged streamwise (left column) and vertical (right column) velocity components for various injection coefficients: $C_\mu = 0$ top row, $C_\mu = 0.051$ middle row, $C_\mu = 0.11$ bottom row. Results obtained from 2D-2C PIV in the center plane of the wing $z = 0$ (i.e. including an actuation micro-jet) and $A0A = 0$. The black line represents the $U = 0$ iso-contour, delimiting the recirculation bubble.

expands for about 5% of the chord length downstream, which represent about one trailing edge diameter and is a typical bluff body recirculation bubble size.

When the control is on, the presence of the micro-jet flow is evident from the yellow trace that is left in the streamwise velocity iso-contours. Contrary to what was originally expected, the micro jet shows a limited turning angle around the trailing edge Coanda surface: it separates rather early from the wall. This is due to a combination of a too high microjet height relative to the Coanda surface radius, and three dimensional effects from the finite span of the

discrete actuation slots [13, 11]. Nevertheless, we can see from figure 4 that the actuation diminishes the overall size of the recirculation bubble and displaces the wake towards the high pressure side of the wing, which is highlighted from the change of sign of the vertical velocity component in the wake (see figure 4 (Right)). Therefore, even if the actuation do not seem to perform as initially expected and that the circulation control can probably be improved using a better suited microjet/Coanda-surface pair geometry, the actuation solution proposed here has a strong effect on the flow and it will be used later to analyze the dynamic response of the flow over the blade for pre-stall configurations (see section 5).

3.1.2. Cross-flow velocity field

As presented in the section 2 the fluidic actuation is three dimensional in our study, hence we need to verify how it performs along the span and seek for possible three dimensional effects.

The cross-flow velocity fields taken at $x/C = 1.03$ of the natural and actuated ($C_\mu = 0.11$) cases are presented in figure 5 (Left and Right respectively). The iso-contour maps represent the streamwise (top row), vertical (middle row) and spanwise (bottom row) velocity components.

It is evident, from figure 5 (top right), that the micro-jet locally diminishes the recirculation bubble, right under the micro-jet. This induces spanwise cells of recirculating flow.

At the streamwise position of the Stereo PIV measurement (i.e. $x/C = 1.03$) and around the microjet, the actuation increases both the downwards and upwards vertical velocity coming from the suction and pressure sides of the profile respectively (see figure 5 (midle row)).

Finally, the presence of the microjet in the flow field forces the incoming flow to circumvent this fluidic obstacle by turning away on its left and right. This explains the cells of the negative and positive spanwise velocity component that can be seen in figure 5 (bottom row) next to the micro-jet axis location. It is also clear from this figure that the flow in the recirculation area is also altered

by the presence of the microjet. The recirculating flow cells that are created in the spanwise direction are three dimensional, with non negligible spanwise recircualting motion.

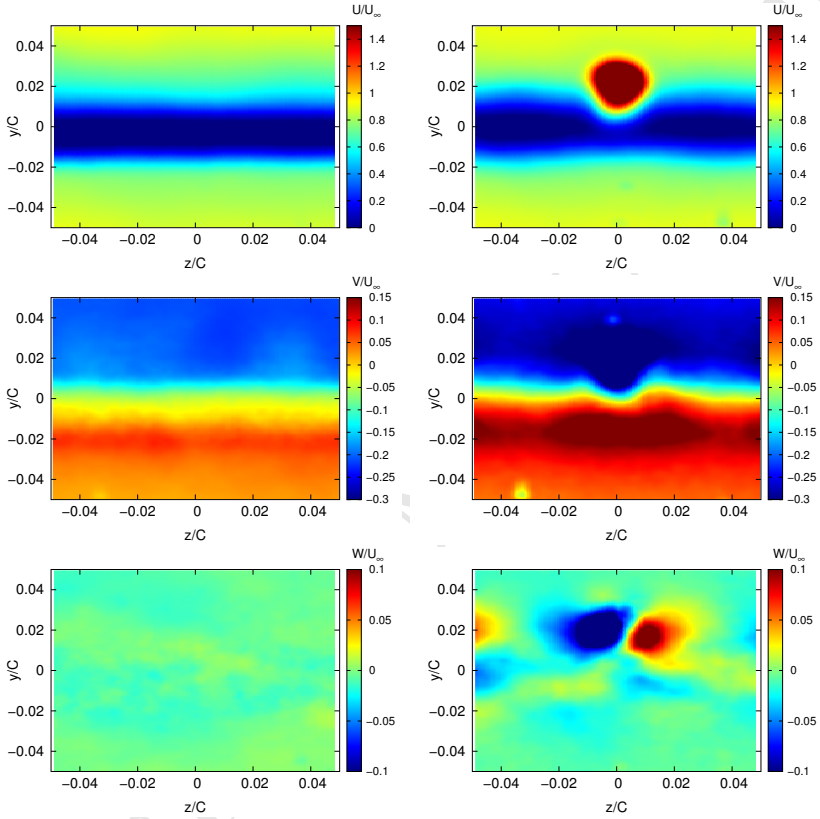

Figure 5: Cross-flow velocity fields taken at $x/C = 1.03$ and $AOA = 0$ for the natural (left column) and for the actuated $C_\mu = 0.11$ (right column) cases. The iso-contour maps represent the streamwise (top row), vertical (middle row) and spanwise (bottom row) velocity component.

To summarize, we have shown that the proposed circulation control system affects the averaged flow field by reducing and by imposing a three-dimensional effect on the recirculation area behind the trailing edge. It has also been shown that these effect are localized in the neighboring area of the microjet main axis. In the following, we want to provide a quantification of the actuation effect on

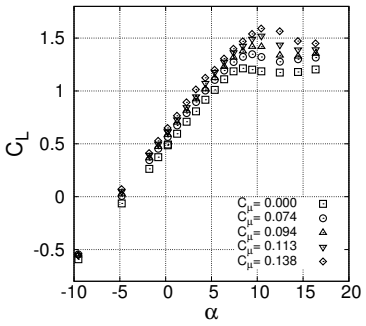

Figure 6: Comparison of actuated versus non-actuated lift curves for the current wing. (left) 10m/s

the lift and drag to relates the observed flow modifications to the eventual gains in aerodynamics performance.

4. Aerodynamic performances/steady state response

4.1. Controlled aerodynamic performances

In figure 6 we present a comparison of the lift curves for different actuation intensities (*i.e* C_μ). The unmanipulated lift curve shows the expected trends for this kind of profiles: a linear lift relation with the AOA for $\alpha \leq \alpha_{sep}$, followed by a saturation for AOA over α_{sep} corresponding to the start of the boundary layer separation from the upper surface of the blade at the trailing edge of the profile.

From this figure, we can see that the actuation has numerous effects on the lift curves. First of all, as expected from previous circulation control attempt, the lift is increased for all angles of attack [44, 21]. This is an important characteristic if one aims at controlling the lift perturbations created by external wind gusts for example. It is also clear from the C_L curves that the actuation plays a significant role in progressively delaying the threshold angle at which the onset of boundary layer separation, α_{sep}, occurs at the trailing edge [32]. It should be noted however that it was not possible with the available blade design to blow jets that decrease lift. A new design is under progress for this purpose and only

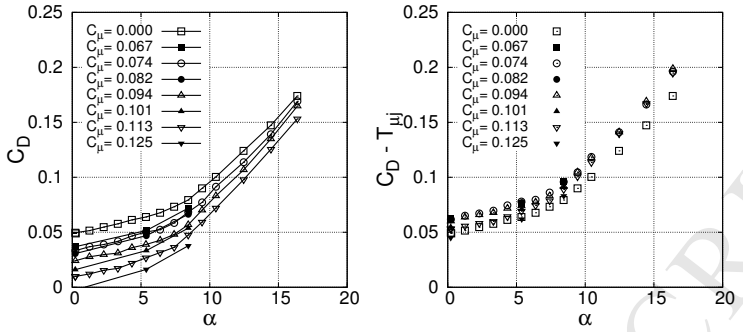

Figure 7: Comparison of actuated versus non-actuated drag curves for the current wing (left). Thrust compensated drag (left)

alleviation of gust that increase wind speed are considered here.

Another observation that can be made from figure 6 is that the static gain is not only dependent on the actuation strength C_μ but also on the flow state (*i.e.* the angle of attack). As can be seen, much more lift is gained after the threshold angle α_{sep} than at attached flow regimes ($\alpha \leq \alpha_{sep}$). This behavior was already observed for various CC devices [45], therefore showing that the currrent CC strategy works with the same principles as what can be found in the litterature. Note however that the maximum gain seems to be located around $\alpha = 10^\circ$ and reduces for higher AOA.

In figure 7 left we present a comparison of the C_D curves for different C_μ. At a first glance, one could think that the control decreases the drag of the profile. However, this is a simple microjet thrust effect. Indeed, each individual microjet acts as a small nozzle that creates thrust in the opposite direction of drag, that can be measured with zero free stream velocity. By removing this thrust effect on the drag measurements, drag curves overlap for all controlled cases (see figure 7 right), showing that the fluidic control has little additionnal effect on the blade drag.

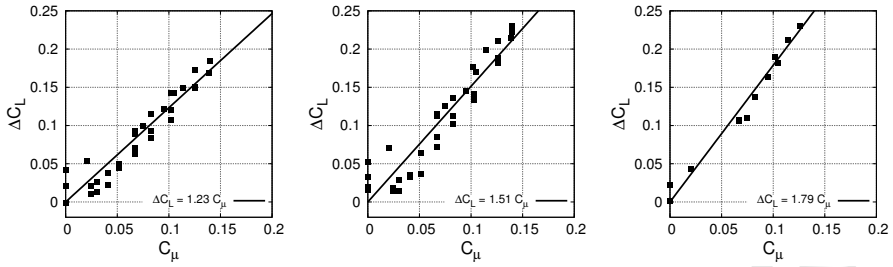

Figure 8: Lift coefficient as function of injection coefficient for $\alpha = 0$ (left), $\alpha = 5$ (center), $\alpha = 8$ (right).

4.2. Sensitivity of actuation

We plot in figure 8 the lift coefficient gain against C_μ for various AOA in the attached regime (i.e. $\alpha \leq \alpha_{sep}$). It is clear that the control gives a linear change in lift for all presented AOA. As stated earlier, the relationship between the micro-jet stagnation pressure and C_μ can be well approximated by a linear relation. Since the relation between C_μ and the micro-jet generating pressure is almost linear (see dedicated previous section), it means that the lift increment due to the actuation is directly proportional to the pressure set in the micro-jet stagnation chamber. This is an interesting consideration for a future feedback control strategy because pressure is a quantity easily measured.

We present on the same figures linear regressions of the measured lift increments. We provide the estimated slope $\frac{\partial \Delta C_L}{\partial C_\mu}$ in the legends of figure 8 and we see that the actuation efficiency is greater for higher angle of attack (from left to right). Note that this trend was also obsered by Troshin and Seifert [30] in a different control configuration. In our case, the natural position of the stagnation point at the trailing edge moves upstream with increasing AOA. This provides more room for the control to displace it downstream, allowing for more circulation changes at higher AOA.

4.3. Discussion on the performance of the current actuation

The comparison of performances with literature is a difficult exercise because of the variety of the different techniques that were used to manipulate

lift. In a review, Greenblatt and Wygnanski [45] proposed two main parameters to evaluate the performances of various actuation devices proposed in the literature. The first one $\Delta C_{L,max}$ corresponds to the gain in maximum lift, and the second one is the maximum post-stall lift gain ΔC_L. We will only use the first one here, since we do not deal with stalled cases in our current study. For example, Seifert *et al* [44] reported a 21% increase of $\Delta C_{L,max}$ for a $C_\mu = 0.001$ using a 2D continuous injection on a flapped NACA 0015 airfoil. From figure 6 we can see that the current actuation device offers a $\Delta C_{L,max}$ of 32% but for a $C_\mu = 0.139$. Additionnaly, Cagle and Jones [20] and Jones et al. [21] used the ratio of lift gain over injection coefficient $\frac{\Delta C_L}{\Delta C_\mu}$ to evaluate the actuation efficiency at a given AOA. They reported a ratio of 50 at $\alpha = 0^\circ$, for a similar concept of lift control but using 2D actuation. Here, we measured a more modest but non negligible $\frac{\Delta C_L}{\Delta C_\mu}$ of 1.29 at the same AOA.

It is believed that these discrepancies are due to the three-dimensional actuation performed in our study. Let's assume that the circulation control is localized in span along the 2D sections of the foil where the micro-jets exists, which is not a strong assumption given the observations made in the previous section. We can therefore recompute the lift gain using the sum of the individual orifice spans, l_a, instead of the wing span, L, as follows: $\Delta C_{L,max2D} = \Delta C_{L,max} \cdot L/l_a$. This leads to a gain of 840% of $\Delta C_{L,max2D}$ at $C_\mu = 0.139$ corresponding to a non negligible 6% increase of $\Delta C_{L,max2D}$ for $C_\mu = 0.001$. This is closer to the reported gains of Seifert et al. [44]. Similarly, we then have a 2D lift to momentum coeficient ratio of $\frac{\Delta C_{L,2D}}{\Delta C_\mu} = 26$, which is of the same order of magnitude than the results of Cagle and Jones [20].

This shows that the chosen actuation method performs in a comparable manner as the different techniques reported in the literature and confirms that most of the lift gain is actually obtained through local modifications of the circulation, as we inferred from the observations of the PIV results in the previous section.

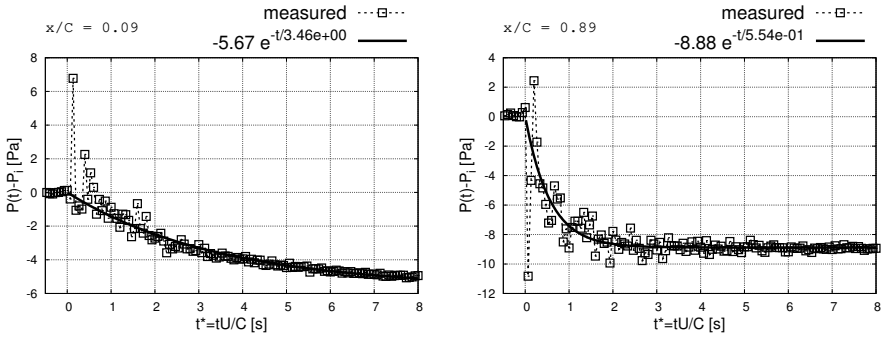

Figure 9: Pressure step response to actuation on the upper side of the wing at $x/C = 0.09$ (left) $x/C = 0.89$ (right). The results are presented for $C_\mu = 0.139$ and $\alpha = 0$.

5. Dynamic response

5.1. Phase locked pressure response

Figures 9 shows pressure responses to a step in actuation, measured at two locations along the chord of the wing suction side at $\alpha = 0$ corresponding to the trailing egde area (right) and the leading edge area (left). These step responses where obtained by averaging 100 different uncorrelated realizations. As can be seen, all the responses can be approximated to a response from a first order Ordinary Differential Equation (ODE) system (see equation 3). Also, the measured responses show a different dynamic response depending on its location on the chord. Fastest responses (i.e. lowest response time) and highest gains are observed near the trailing edge of the wing close to the location of the actuator.

For higher angles of attack, when the boundary layer separates from the surface at the trailing edge of the blade, different responses are observed. The figure 10 presents pressure step responses obtained at $\alpha = 14$ and $C_\mu = 0.138$. As can be seen, the pressure response for detached flow cases no longer resembles to a response of a first order ODE system. At these AOA, it is possible to recognize an under-dumped second order ODE system response, with a small overshoot.

In order to have a better overview of the multiple outputs of the system, we

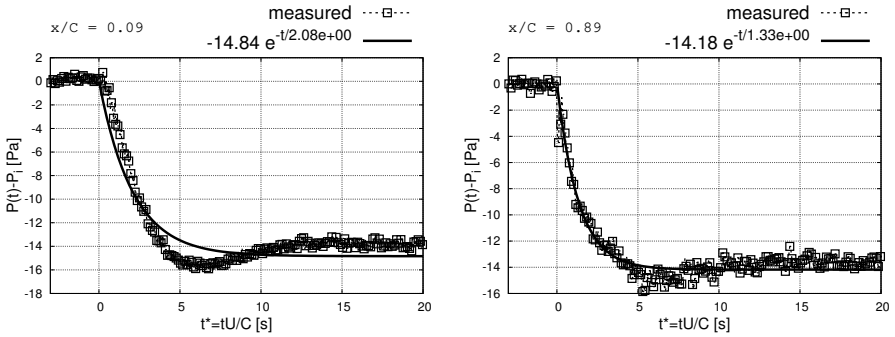

Figure 10: Pressure step response to actuation on the upper side of the wing at $x/C = 0.09$ (left) $x/C = 0.89$ (right). The results are presented for $C_\mu = 0.139$ and $\alpha = 14$.

fitted the following first order type response for each pressure response:

$$\Delta P(\mathbf{x}, t) = P(\mathbf{x}, t) - P_i = K\ u(t)\ \left(1 - e^{-t/\tau}\right), \tag{3}$$

where P is the pressure, t the time, $K = K(\mathbf{x})$ the steady state gain, $\tau = \tau(\mathbf{x})$ the time constant of the system (i.e. time to reach 63% of the steady state), $P_i = P_i(\mathbf{x})$ the initial value of the pressure over the upper surface of the blade and u(t) is the control input that is equal to unity when actuation is ON and to zero otherwise. Typical fitted results are given in figures 9 and 10. Even though, this response type is not adapted to the pressure response at high angles of attack, it can be seen in figure 10 that the error between the fitted function and the measured response is relatively small such that the gains and response times obtained are fairly representative of the real system. Results can be separated in two areas. The first one near the actuator were a significant peak, proportional to the control input C_μ, is observed and should induce an increase of the pitching moment as usually observed in CC devices [46]. The second area is plotted in figure 11 using the different dimensionless steady state gains found around the chord of the profile for different control inputs (i.e. C_μ) at $\alpha = 0$.

First of all, contrary to what is reported by many authors [26, 27, 28], we didn't find significant differences between dynamic responses to an actuation step ON

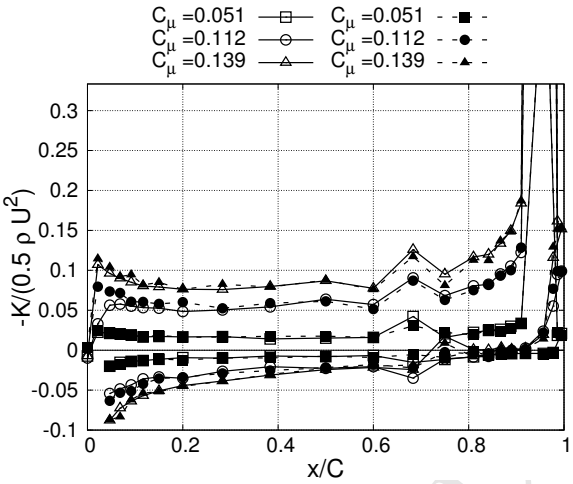

Figure 11: Evolution of the gains K with the chord for varying actuation intensities, the vertical axis was chose to cut-off the very high gains obtained in the neighborhood of the actuator, open and closed symbols are for opening and closing actuation respectively

(open symbols of figure 11) and an actuation step OFF (closed symbols of figure 11). The main difference between these studies is the initial state of the flow before control. In the results of figure 11 the flow is attached all the time while in the other studies the flow is either initially separated [26, 27], or the final targeted state is the flow separation [28].

The second important observation is a clear effect of the actuation intensity on the steady state gains: the stronger the actuation, the higher the steady state gain. This is in agreement with the previous results of the balance measurements (see figure 8). At last, results show that the respective contributions of both areas (i.e. nearby the actuation and around the chord) to the integrated gain (lift coefficient) are of the same order of magnitude. Therefore, the actuation used in this study, although very local, modifies the overall pressure field around the wing, similarly as can be found in other circulation control configurations [21, 20].

Figure 12 shows the dimensionless time constants τ found around the chord of the profile for different control inputs. This response time corresponds to the

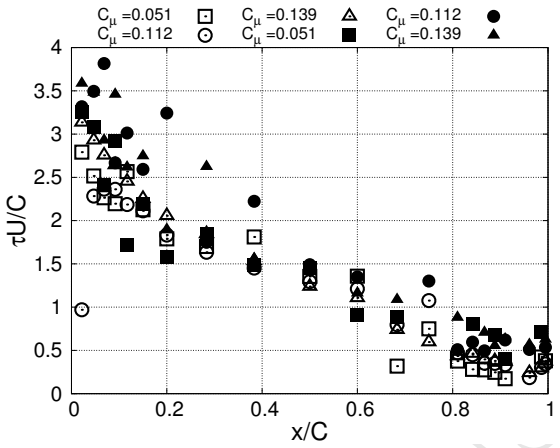

Figure 12: Distribution of the time responses τ with the chord for varying actuation intensity at $\alpha = 0$. Open and closed symbols are for opening and closing actuation respectively

time needed to reach 63% of the steady state. The 99% steady state response time, τ_{99}, is three times τ. τ_{99} is found to range from 1.5 to 13.5 convective times. Note that previous studies did not investigate the response time around the chord but rather close to the actuation, however, for locations close the leading edge (or away from the actuation) the response time of pressure is of the same order of magnitude of the one reported in the literature in separated flow over a wing [24, 22] and in detached boundary layer flow [28, 29].

Results of the present study show a clear trend of the response time around the chord. For all input values, the time constant is increasing with the distance from the actuation. If the static gains were homogeneously distributed around the profile, no steady states change in pitching moment is expected. However, the fact that the pressure takes longer to establish far from the actuation indicates that transient pitch torque is created during the establishment of the modified circulation. This is rather important behavior for final application, that might also be found in other CC devices.

We present in figure 13 the chordwise distribution of K and τ measured with $C_\mu = 0.139$ for varying AOA. As expected for the lift curve presented in figure 6, the gain depends highly on the AOA on the suction side, while almost no

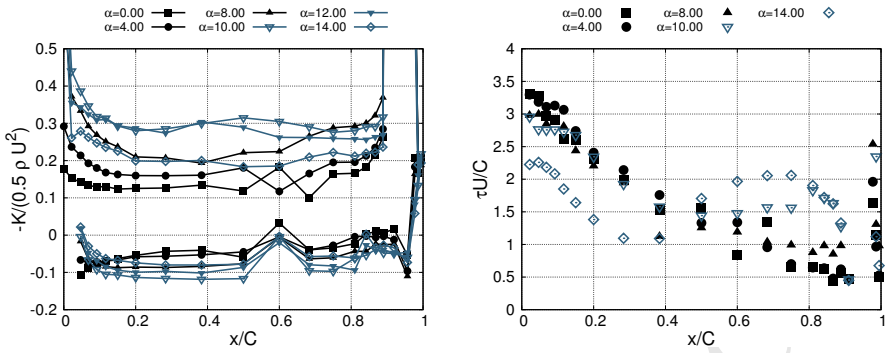

Figure 13: Left: chordwise evolution of the gain K for different angles of attack. Right: evolution of the response time τ with the chord for different angles of attack. On both figure attached regimes are presented with black symbols, whereas blue symbols represent detached flow regimes.

effect is observed on the pressure side. The highest gain is found for $\alpha = 10$ in good agreement with the gain of C_L found in figure 6. For higher AOA, the gain deacreases, also in good agreement with figure 6.

Regarding the response time of pressure, no effect of the angle of attack on the response time is perceived for attached flow cases. As previously observed, longer response times are measured for locations farther from the actuator. This observation is no longer valid for detach regimes where the response time seems to be more evenly distributed along the chord. The $\alpha = 10^\circ$ results show that for $x/C < 0.6$ the response times are comparable to smaller AOA whereas for $x/C > 0.6$ the response times are increased compared to the attached flow cases. For $\alpha = 14$, the response times are clearly slowed near the trailing ege (i.e. for $x/C > 0.5$) and accelerated near the leading edge (i.e. for $x/C > 0.5$) inducing a relativelly constant time response over the chord. This is an indication that the separated flow possesses a different dynamics than the attached one.

The results of this section show that the dynamic response of the flow over an airfoil is strongly dependent on the presence of flow detachment on the suction side of the wing. Even though no direct measurement of the pitching moment was performed, the results of this section show that a transient pitching mo-

ment is expected from the local response time of the pressure that depends on the distance to the actuation. Hence, the fact that the local response time of pressure depends on the distance to the actuation is an interesting result that should be beard in mind.

Nevertheless, it seems that the pressure response to the actuation can be reasonably approximated by typical first order system types, demonstrating that the dynamics of pressure establishment remains relatively simple.

5.2. Phase locked C_L response

From the former phase locked pressure step responses, it is possible to build the corresponding lift step responses by simply integrating the pressure field on the wing surface :

$$C_L(t) = \frac{1}{S_{ref}} \int_S C_p(\mathbf{x}, t) d\mathbf{x} \tag{4}$$

where $C_p = \frac{P - P_\infty}{0.5 \rho U_\infty^2}$ the pressure coefficient with $\mathbf{x}$ the projection of the profile skin coordinates in the streamwise direction. The lift response $\Delta C_L(t)$ can then be directly obtained by spatially integrating the measured pressure response at each time step:

$$\Delta C_L(t) = \frac{2}{\rho U_\infty^2 S_{ref}} \int_S \Delta P(\mathbf{x}, t) \, d\mathbf{x}, \tag{5}$$

where $\Delta P(\mathbf{x}, t)$ is defined in equation 3.

The measured lift step responses are plotted in figure 14 for the three different momentum coefficients at $\alpha = 0$. The lift gain is normalized by the steady state gain and all the lift responses collapse onto a single curve corresponding to a typical step response from an ODE system. A least-square approximation of equation $C_L(t) = 1 - K_L e^{-t/\tau_L}$ is performed and plotted against experimental measurement points. The response time to reach 63% of the steady state is found of the order of one convective time $\tau = \frac{U_\infty}{C}$ while the response time to reach 99% of the steady state is more than 3 convective times.

Theoretical lift response to gusts for attached flow cases is usually given by the

Küssner's function [47] obtained using potential flow theory. The derived lift response can be approximated by a three exponential term function [48]:

$$C_{Lg}(s) = 1.0 - 0.236e^{0.058s} - 0.513e^{0.364s} - 0.171e^{2.42s}, \quad (6)$$

where $s = t\frac{C}{2U_\infty}$ is the dimensionless time based on the freestream velocity and the half chord. The former equation is also reported on figure 14.

As can be seen, the measured lift response is faster than what is theoretically predicted. There might be several reasons why the theory fails in recovering the measured response time. First of all the theoretical model uses inviscid flow and thus cannot model the fact that the CC actuation modifies the flow separation on the trailing edge. Moreover, the theory and the experiment do not use identical type of perturbation: in the theoretical model the gust is modeled as a local camber modification of the wing whereas in the experiment the perturbation is introduced at the trailing edge. It is therefore difficult to conclude on the observed differences but it must be noticed that blade profiles lift might have a faster response time than what is generally considered for fluid/structure interaction.

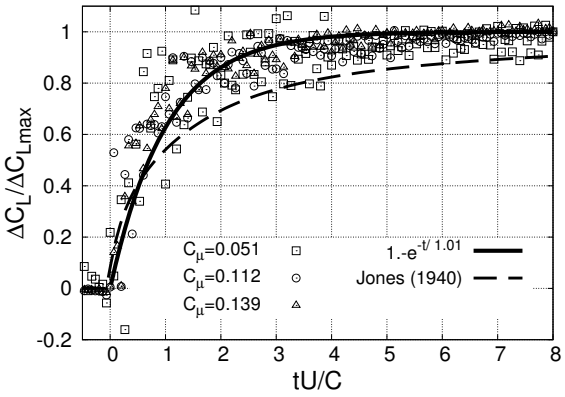

Figure 14: Step responses of the lift coefficient C_L for different actuation intensity obtained by integrating all the measured pressure responses at $\alpha = 0$.

The measured lift step responses obtained for varying angle of attack are

presented in figure 15. As can be observed, as long as the flow is attached (*i.e.* $\alpha < 10^\circ$) all the lift responses are similar and almost collapse onto a single curve, suggesting that the lift response of the entire attached configuration can be approximated by a first order response. The first order response previously identified is also plotted on the same figure and a satisfactory agreement with the measured responses is obtained showing that the response time, τ, of the attached lift in our case is of the order of 1 convective time $\tau = C/U_\infty$.

For detached cases, the response curves are different and show an overshoot of lift before it reaches the steady state value, which is a typical behavior of under-damped second order system. The response time of lift at these angles of attack is therefore slightly longer than for attached cases. As a matter of comparison, we derived the step responses from the indicial lift response measured by Colonius and Williams [24] on a semi-circular wing with leading edge flow separation. This curve is reproduced on figure 15 and also exhibits an overshoot but with a slower response than for our cases for which only trailing edge flow separation occurs.

These result may suggest that the lift response strongly depends on whether the flow is separated or attached but also on how/where it separates from the wall. Separation close to the trailing edge seems to provide faster responses than separation at the leading edge of the wing.

5.3. Comparison with turbulent scales

The response time scale observed in the previous paragraph has to be compared with the times scales of perturbations that can be found in the atmospheric boundary layer. Typical spectrum of atmospheric boundary layer velocity fluctuations are given in figure 16, based on the formula given by Kaimal *et al* [1]. This spectrum is plotted against a reduced frequency representative of the characteristic scales of an existing wind turbine blade with chord length of 1m and velocity of 60m/s. As can be seen, most of the velocity perturbations are low frequency with respect to the blade time scales: the peak frequency of all the perturbations are found below $St < 0.1$ for all the 3 velocity components. Since

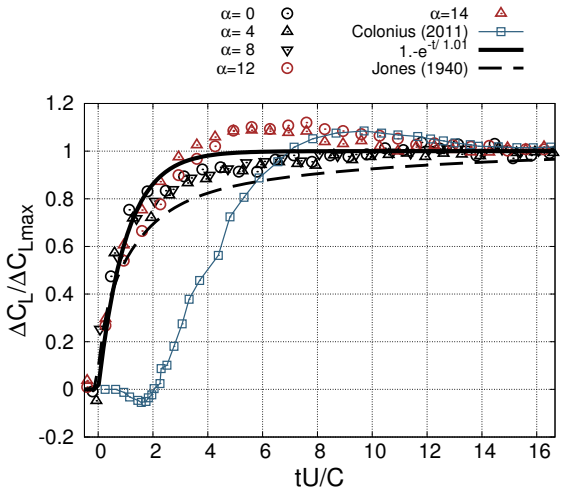

Figure 15: Step responses of the lift coefficient C_L obtained by integrating all the measured pressure responses for various AOA at $C_\mu = 0.14$ compared with theoretical functions as well as other experimental results. For sake of clarity only one point over 10 is plotted.

the open-loop control system has a characteristic frequency of $St = 1$, it is clear that the proposed system is rapid enough to account for those scales. This is illustrated in figure 16, where the shaded area corresponds to frequencies above the cut-off frequency of the open-loop system, and the transfer function of the lift system is presented in dark-grey. It should be mentioned that the response time of closed-loop systems can be made faster than the open-loop one, hence ensuring that it is physically possible the account for external perturbations at the blade scale.

6. Closed-loop control

6.1. Control Modeling

From the results of the former section a numerical model of the system can be built to evaluate the performances of a feedback controller. Since the system can be represented by a first order ODE system, a PID controller should be able to handle the system [29]. However, one has to notice that the present fluidic actuators are not proportional: valves are either open or closed providing a fixed

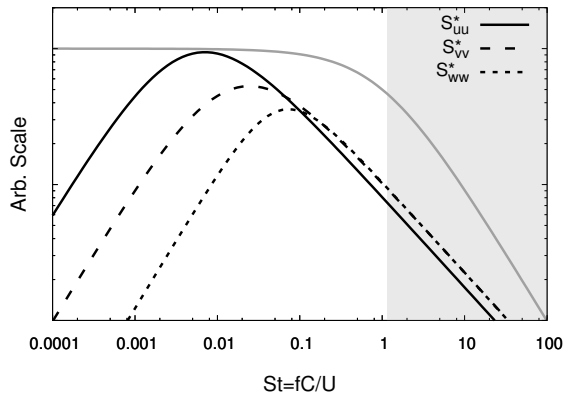

Figure 16: Spectrum velocity perturbations in an atmospheric boundary layer taken at an altitude of $z = 80$m and average velocity of $8m/s$. The frequency is reduced by a wind turbine blade length and velocity scales. The grey curve represents the efficiency of the open-loop control system: beyond $St = 1$ the control system becomes inefficient.

output amplitude at each actuation. Duty cycle changes at a fixed actuation frequency can be used to mimic changes in injected mass flow rate [49, 29], this is similar to switching a high voltage in order to provide lower voltage power supply in electronics.

The present actuation system (valves with pneumatic circuit) have a maximum response time of around 0.007 seconds that was measured on bench experiments using hot-wire measurements. The controller is thus more than ten times faster than the response of the system, $\tau_{99} = 3 \times C/U_\infty \approx 0.09$ seconds. To take into account the binary operation of the valve, we have developed an additional model. This allows us to evaluate the effect of binary actuation on lift control compared to proportionnal one. The overall model is presented in figure 17, where **PI** is the proportional-integral controller, **H** is the lift transfer function as identified in the former section and **V** is our valve model. In this figure C_{L0} is the lift setpoint, C_{Lp} the lift perturbation, C_μ the actuation signal and C^*_μ the more realistic actuation signal with solenoid valve type properties.

The **PI** controller was designed according to the Ziegler-Nichols rules, and implemented with an anti-windup. The lift transfer function that is being used

is presented in figure 17 (right). The valve system **V**, is actually a binarization of the output of the **PI** controller. The valve model is constrained so that the valves can only change state after a minimum duration corresponding to half their minimum response period of 3.5 ms. To ensure a more realistic and smooth actuation signal, the pressure rise in the plumbing was modeled by a first order dynamical system with a reponse time of 3.5 ms. Hence, the total response time of the modeled actuation sytem is 7 ms, in agreement with what was experimentally observed. A typical closed loop control result is shown

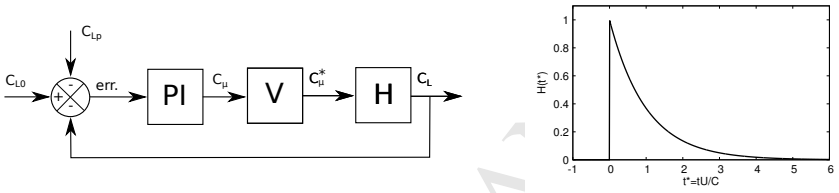

Figure 17: Diagram of the feedback-loop model developed to simulate the control system (letf). Transfer function H used in the feeback-loop model (right).

in figure 18 (left). The setpoint was changed from $C_{L0} = 0$ to $C_{L0} = 0.1$ at $t^* = 50$. At the same time, an external sinusoidal pertubation was imposed: $C_{Lp} = 0.05\cos(w_p t^*)$ with w_p the perturbation frequency chosen according to figure 16. As can be seen, even with a binarized actuation the actuator is still able to minimize the effect of the perturbations so that the output lift stays close to the setpoint.

It is clear form figure 18 that the control could not entirely remove the lift perturbation. The remaining lift oscillations are due to the non-proportional behavior of the valves, indeed if the valves are modeled as ideal ones (*i.e.* have an infinitesimal reaction time), the incoming perturbations could be entirely removed as can be seen in figure 19.

Another important point that arises from the fact that our actuators are binary, is that parameters of the controller (i.e. PID) have very limited impact on the efficiency of the control. This is obvious considering that the actuation signal computed by the PID is actually binarized *a posteriori* by the valves. This

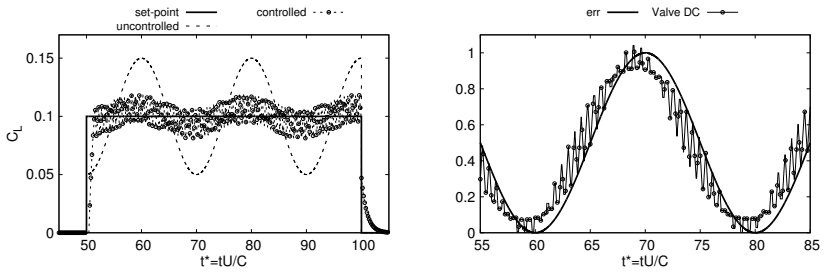

Figure 18: Example of simulated lift control in the time domain (left). Comparison of normalized lift perturbation with the actuation signal duty cycle (right). The actuation is started at $t^* = 50$.

means that no fine tuning of the controller parameters is actually needed when electromagnetic valves are used.

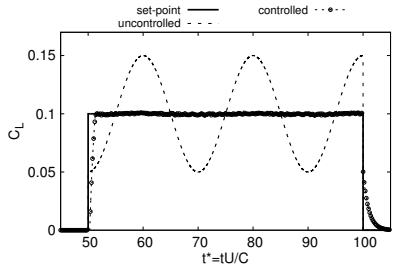

Figure 19: Example of simulated lift control using ideal valves. The actuation is started at $t^* = 50$.

6.2. Experimental results

Based on the encouraging results obtained using the model of the previous section, an experiment has been designed to test the closed-loop control. The wing is mounted on a motorized bench allowing to vary the angle of attack, which acts as a perturbation in lift as sketched in the figure 20 (right). The profile is equipped with 15 pressure sensors on the suction side of the wing which serve to estimate the lift. Note that no sensor was placed on the pressure side of the wing. Since the lift setpoint is evaluated by integrating the average pressure

distribution around the wing at a given angle of attack, this estimation of the lift information (using the suction side only) was found enough for an efficient and simple proportional controller implementation.

Since the actuation can only increase the lift, the perturbation consists in a sinusoidal variation of α defined as follows:

$$\alpha(t) = \alpha_0 - \Delta\alpha \cdot \sin(2\pi f_\alpha t), \tag{7}$$

where α_0 is the AOA at which the lift setpoint is measured, $\Delta\alpha$ is the amplitude of the perturbation and f_α the oscillation frequency. The oscillation frequency is chosen so that $St_\alpha = \frac{f_\alpha C}{U} = 0.003$. It is at the same time low enough to avoid dynamic stall effect and/or hysteresis effect that can be expected to appear around $St = \frac{f_\alpha C}{U} = 0.1$ [2, 50, 51], but high enough to be representative of scaled atmospheric turbulent perturbations.

The feedback loop used in this experiment is shown in figure 20 (left). The error between measured lift and the setpoint is computed and fed to a proportional controller. The output of the controller is then binarized to a TTL electric signal that can be used to actuate the electric valves. Then a new estimate of lift is computed by integrating the pressure on the wing and compared to the setpoint, hence closing the loop.

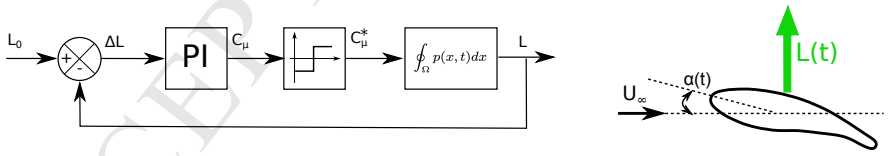

Figure 20: Diagram of the feedback-loop used on the experiment (left), sketch of the external lift perturbation applied to the wing by varying the angle of attack (right).

The results of the closed-loop control in the attached regime are presented in figure 21 for $\alpha_{sp} = 4^\circ$ and $\Delta\alpha = 2^\circ$. Before the control is turned on, the lift oscillates in phase with the perturbation. It is clear that, as soon as the control is ON, the lift oscillations are reduced by 83%, proving that feedback control of lift using fluidic actuation is an efficient method. The results of the

closed-loop control in the separated regime is presented in figure 22. The main difference with the previous results is that there is a phase opposition between the AOA perturbation and the lift output before control. This is expected from the change of slope in the C_L *vs.* α curve for AOA greater than 10°. However, this does not modify the control efficiency which is found of the same order of magnitude.

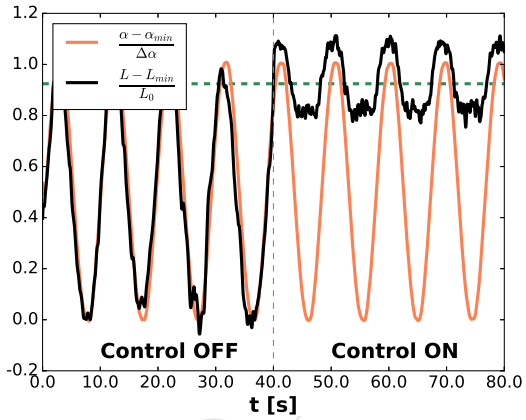

Figure 21: Time traces of normalized lift and angle of attack. The lift controller is set at $t = 40s$. Setpoint measured at $\alpha = 4^\circ$: the flow is attached.

These results not only show the feasibility of feedback lift control but also show that this simple control can be applied even when the regime of the flow over the blade is in the non-linear part of the lift coefficient.

7. Conclusions and Perspectives

An experiment was designed to evaluate the ability of lift control by means of fluidic actuation on a modified the trailing edge of wind turbine blades. At the studied Reynolds number of $2 \cdot 10^5$, the proposed device is able to increase the average lift of the profile with a proportionnal dependance between lift gain and actuation intensity. It was observed that the actuation was more efficient around the flow trailing edge separated regime. PIV measurements were performed to examine the flow modifications indicuded by the actuation, and it

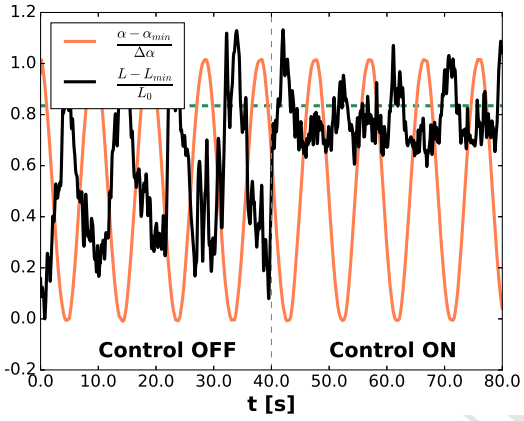

Figure 22: Time traces of normalized lift and angle of attack. The lift controller is set at $t = 40s$. Setpoint measured at $\alpha = 12^\circ$: the flow is separated.

was shown that the lift gain is associated to the pinching of the recirculating flow downstream of the trailing edge.

The dynamics of the lift change was studied and we have shown that the wall pressure dynamics has a time scale that depends on the distance to the actuation. It was also shown that the time scales associated to the establishment of the modified mean flow and the ones associated to the return to the initial state are the same. This behavior is different from the observations made for separated flow control where separation and reattachement usually possess different time scales [26, 27, 28]. We have shown that the lift response also depends on the state of the flow on the suction side of the wing (i.e. no separation, trailing edge separation): the lift response time increases when the flow separation occurs closer to the leading edge.

For attached cases the lift dynamics was shown to be well approximated by a first order ODE system with a characteristic time scale of C/U taken at 63% of the steady-state value, giving a 99% time scale of $3C/U$. When a trailing-edge separation occurs, the response shape can be approximated to a second order ODE system, with an overshoot and a slightly longer time scale. It is noticeable that the time response of the present attached cases is slighly faster than what

was observed for stalled cases [22, 24] and much faster than the theoretical lift response obtained from thin airfoil theory. Moreover, a key information to keep in mind is the difference of 2 orders of magnitude between the slow turbulence time scales of the incomming boundary layer and the faster lift dynamics time scale. This ensures that the control can act fast enough to allieviate some of the load associated with gusts. A model was derived from the observed dynamics allowing to test the control strategies. A model of the binary actuation system was included for more realistic condition purposes. It was shown that a feedback loop control is expected to work even if the actuators are not proportionnal. An experimental evidence of the feasability of lift control is also provided using lift perturbations obtained by variations in angle of attack. Up to 80% of the lift oscillations could be removed for AOA varying within $\pm 2^\circ$, the state of the flow being attached or separated at the trailing edge of the blade. As mentionned earlier in the paper, the lift dynamics is assessed here using trailing edge perturbations at a single moderate Reynolds number and the gust perturbations are mimicked by changes in angle of attack. Some more research efforts are required to investigate both the lift response and control preformance to more realistic perturbations.

Acknowledgments

The authors want to thank the French National Research Agency for supporting this study through the SMARTEOLE project (ANR-14-CE05-0034). Also, the authors would like to thank the PRISME laboratory staff where the wind tunnel experiments presented here were performed.

[1] J. Kaimal, J. Wyngaard, Y. Izumi, O. Coté, Spectral characteristics of surface-layer turbulence, Quarterly Journal of the Royal Meteorological Society 98 (1972) 563–589.

[2] A. Choudhry, R. Leknys, M. Arjomandi, R. Kelso, An insight into the dynamic stall lift characteristics, Experimental Thermal and Fluid Science 58 (2014) 188–208.

[3] M. Melius, R. B. Cal, K. Mulleners, Dynamic stall of an experimental wind turbine blade, Physics of Fluids 28 (2016) 034103.

[4] A. Choudhry, M. Arjomandi, R. Kelso, Methods to control dynamic stall for wind turbine applications, Renewable Energy 86 (2016) 26–37.

[5] D. Castaignet, N. K. Poulsen, T. Buhl, J. J. Wedel-Heinen, Model predictive control of trailing edge flaps on a wind turbine blade, in: American Control Conference (ACC), 2011, IEEE, pp. 4398–4403.

[6] D. Castaignet, T. Barlas, T. Buhl, N. K. Poulsen, J. J. Wedel-Heinen, N. A. Olesen, C. Bak, T. Kim, Full-scale test of trailing edge flaps on a vestas v27 wind turbine: active load reduction and system identification, Wind Energy 17 (2014) 549–564.

[7] J. Ortega Gmez, C. Balzani, Load reduction potential on large wind turbines using active trailing edge flaps, in: Conference of the Wind Power Engineering Community (COWEC), Berlin.

[8] L. Neuhaus, P. Singh, O. Huxdorf, J. Riemenschneider, J. Wild, J. Peinke, M. Hlling, Mitigating loads by means of an active slat, in: Torque.

[9] P. M. Hartwich, E. D. Dickey, A. J. Sclafani, P. Camacho, A. B. Gonzales, E. L. Lawson, R. Y. Mairs, A. Shmilovich, Afc-enabled simplified high-lift system integration study, NASA/CR-2014-218521 (2014).

[10] R. J. Englar, R. M. Williams, Design of a circulation control stern plane for submarine applications, Technical Report, DTIC Document, 1971.

[11] R. J. Englar, Experimental investigation of the high velocity coanda wall jet applied to bluff trailing edge circulation control airfoils, Technical Report, DTIC Document, 1975.

[12] R. J. Englar, Two-dimensional subsonic wind tunnel tests on a cambered 30 percent-thick circulation control airfoil, Naval Ship Research and Development Center. Tech. Note AL-201)(In preparation) ii (1972).

[13] M. Kadosch, Déviation des jets par adhérence à une paroi convexe, Journal de Physique Appliquée 19 (1958) 1–12.

[14] J. Kweder, C. C. Panther, J. E. Smith, Applications of circulation control, yesterday and today, International Journal of Engineering 4 (2010) 411.

[15] A. Dumitrache, F. Frunzulică, H. Dumitrescu, R. Mahu, S. Sivasundaram, Active and passive circulation control as enhancement techniques of wind turbines performance, in: AIP Conference Proceedings, volume 1493, AIP, pp. 330–337.

[16] A. Shires, V. Kourkoulis, Application of circulation controlled blades for vertical axis wind turbines, Energies 6 (2013) 3744–3763.

[17] S. Baleriola, A. Leroy, S. Loyer, P. Devinant, S. Aubrun, Circulation control on a rounded trailing-edge wind turbine airfoil using plasma actuators, in: Journal of Physics: Conference Series, volume 753, IOP Publishing, p. 052001.

[18] A. Leroy, C. Braud, S. Baleriola, S. Loyer, P. Devinant, S. Aubrun, Comparison of flow modification induced by plasma and fluidic jet actuators dedicated to circulation control around wind turbine airfoils, in: Journal of Physics: Conference Series, volume 753, IOP Publishing, p. 022012.

[19] C. Braud, E. Guilmineau, Jet flow control at the blade scale to manipulate lift, in: Journal of Physics: Conference Series, volume 753, IOP Publishing, p. 022031.

[20] C. M. Cagle, G. S. Jones, A wind tunnel model to explore unsteady circulation control for general aviation applications, in: 22nd AIAA Aerodynamic Measurement Technology and Ground Testing Conference, pp. 24–26.

[21] G. S. Jones, S. A. Viken, A. E. Washburn, L. N. Jenkins, C. M. Cagle, An active flow circulation controlled flap concept for general aviation aircraft applications, AIAA paper 3157 (2002).

[22] D. R. Williams, G. Tadmor, T. Colonius, W. Kerstens, V. Quach, S. Buntain, Lift response of a stalled wing to pulsatile disturbances, AIAA journal 47 (2009) 3031–3037.

[23] D. Williams, W. Kerstens, S. Buntain, V. Quach, J. Pfeiffer, R. King, G. Tadmor, T. Colonius, Closed-loop control of a wing in an unsteady flow, AIAA Paper (2010) 2010–0358.

[24] T. Colonius, D. R. Williams, Control of vortex shedding on two-and three-dimensional aerofoils, Philosophical Transactions of the Royal Society of London A: Mathematical, Physical and Engineering Sciences 369 (2011) 1525–1539.

[25] G. Woo, T. Crittenden, A. Glezer, Transitory control of a pitching airfoil using pulse combustion actuation, in: 4th Flow Control Conference, p. 4324.

[26] A. Darabi, I. Wygnanski, Active management of naturally separated flow over a solid surface. part 1. the forced reattachment process, Journal of Fluid Mechanics 510 (2004) 105–129.

[27] A. Darabi, I. Wygnanski, Active management of naturally separated flow over a solid surface. part 2. the separation process, Journal of Fluid Mechanics 510 (2004) 131–144.

[28] R. Mathis, A. Lebedev, E. Collin, J. Delville, J.-P. Bonnet, Experimental study of transient forced turbulent separation and reattachment on a bevelled trailing edge, Experiments in Fluids 46 (2009) 131–146.

[29] T. Shaqarin, C. Braud, S. Coudert, M. Stanislas, Open and closed-loop experiments to identify the separated flow dynamics of a thick turbulent boundary layer, Experiments in fluids 54 (2013) 1448.

[30] V. Troshin, A. Seifert, Performance recovery of a thick turbulent airfoil using a distributed closed-loop flow control system, Experiments in fluids 54 (2013) 1443.

[31] P. Devinant, T. Laverne, J. Hureau, Experimental study of wind-turbine airfoil aerodynamics in high turbulence, Journal of Wind Engineering and Industrial Aerodynamics 90 (2002) 689–707.

[32] S. Balériola, Etude expérimentale dactionneurs plasma surfaciques pour optimiser les performances aérodynamiques dun profil éolien, Master's thesis, University of Orléans, France, 2015.

[33] S. Aubrun, P. Leroy, A.and Devinant, Aerodynamic loads fluctuations alleviation by circulation control on wind turbine blades, in: 50th 3AF International conference on applied aerodynamics,Toulouse, France.

[34] M. O. Hansen, Aerodynamics of wind turbines, Routledge, 2015.

[35] D. Tang, P. G. Cizmas, E. Dowell, Experiments and analysis for a gust generator in a wind tunnel, Journal of aircraft 33 (1996) 139–148.

[36] N. Reinke, T. Homeyer, M. Hölling, J. Peinke, Flow modulation by an active grid, arXiv preprint arXiv:1703.00721 (2017).

[37] R. J. Adrian, Particle-imaging techniques for experimental fluid mechanics, Annual review of fluid mechanics 23 (1991) 261–304.

[38] C. Willert, Stereoscopic digital particle image velocimetry for application in wind tunnel flow s, Meas. Sci. Technol. 8 (1997) 1465–1479.

[39] A. K. Prasad, Stereoscopic particle image velocimetry, Exp. In Fluids 29 (2000) 103–116.

[40] H. Huang, D. Dabiri, M. Gharib, On errors of digital particle image velocimetry, Measurement Science and Technology 8 (1997) 1427.

[41] F. Scarano, Iterative image deformation methods in piv, Meas. Sci. Tech. 13 (2002) R1–R19.

[42] B. Wieneke, K. Pfeiffer, Adaptive piv with variable interrogation window size and shape, 15th Int Symp on Applications of Laser Techniques to Fluid Mechanics Lisbon, Portugal (2010).

[43] J. Westerweel, F. Scarano, Universal outlier detection for piv data, Experiments in Fluids 39 (2005) 1096–1100.

[44] A. Seifert, T. Bachar, D. Koss, M. Shepshelovich, I. Wygnanskil, Oscillatory blowing: a tool to delay boundary-layer separation, AIAA journal 31 (1993) 2052–2060.

[45] D. Greenblatt, I. J. Wygnanski, The control of flow separation by periodic excitation, Progress in Aerospace Sciences 36 (2000) 487–545.

[46] R. Englar, G. Jones, B. Allan, J. Lin, 2-d circulation control airfoil benchmark experiments intended for cfd code validation, in: 47th AIAA Aerospace sciences meeting including the new horizons forum and aerospace exposition, p. 902.

[47] H. G. Küssner, Zusammenfassender bericht über den instationären auftrieb von flügeln, Luftfahrtforschung 13 (1936) 410–424.

[48] R. T. Jones, The unsteady lift of a wing of finite aspect ratio (1940).

[49] B. G. Allan, J.-N. Juang, D. L. Raney, A. Seifert, L. G. Pack, D. E. Brown, Closed-loop separation control using oscillatory flow excitation, Technical report, NASA/CR-2000-210324, ICASE report 2000-32 (2000).

[50] W. McCroskey, K. McAlister, L. Carr, S. Pucci, An experimental study of dynamic stall on advanced airfoil sections. volume 1: Summary of the experiment (1982).

[51] K. McAlister, S. Pucci, W. McCroskey, L. Carr, An experimental study of dynamic stall on advanced airfoil section. volume 2: Pressure and force data (1982).

- Lift control using fluidic actuation at the trailing edge of a windturbine blade
- Investigation of lift dynamics on a windturbine blade
- Experiemental closed-loop control of lift